PAPER

Characterization of phonon thermal transport of $Ti_3C_2T_x$ MXene thin film

IOP Publishing Journal of Physics: Condensed Matter
J. Phys.: Condens. Matter **34** (2022) 155704 (8pp) https://doi.org/10.1088/1361-648X/ac4f1c

Characterization of phonon thermal transport of $Ti_3C_2T_x$ MXene thin film

Hao Wu[1,5], Jiaxin Gu[1,5], Zhongcheng Li[1,5], Wenxiang Liu[1], Hua Bao[2], Huan Lin[3] and Yanan Yue[1,4,*]

[1] Key Laboratory of Hydraulic Machinery Transients (MOE), School of Power and Mechanical Engineering, Wuhan University, Wuhan, Hubei, 430072, People's Republic of China
[2] University of Michigan-Shanghai Jiao Tong University Joint Institute, Shanghai Jiao Tong University, Shanghai 200240, People's Republic of China
[3] School of Environmental and Municipal Engineering, Qingdao University of Technology, Qingdao, Shandong, 266033, People's Republic of China
[4] Department of Mechanical and Manufacturing Engineering, Miami University, Oxford, OH, 45056, United States of America

E-mail: yyue@whu.edu.cn

Received 20 October 2021, revised 17 January 2022
Accepted for publication 26 January 2022
Published 10 February 2022

Abstract

Two-dimensional MXene materials with high electrotonic conductivity, good chemical stability, and unique laminar structure show great potential in the field of electrochemistry. In contrast to the widely concerned electrical properties, studies on the thermal properties of MXene materials are very limited. This paper presents a comprehensive analysis of the thermal properties of $Ti_3C_2T_x$ MXene thin film. Thermal diffusivity and thermal conductivity of $Ti_3C_2T_x$ films are characterized by the transient electro-thermal technique. The experimental results show a 16% enhancement in thermal conductivity when the temperature is increased from 307 K to 352 K. The phonon transport contributes substantially to thermal conductivity compared with electron transport. Molecular dynamic simulation is employed to further investigate the role of phonon thermal transport of Ti_3C_2 layer. It is found that the combined effect of specific heat capacity, stacking structure and internal stress states is responsible for the thermal transport performance of $Ti_3C_2T_x$ MXene thin film.

Keywords: thermal conductivity, MXene, temperature dependence

(Some figures may appear in colour only in the online journal)

1. Introduction

In recent years, the development of new energy storage and conversion technologies has become a trend in sustainable energy. Electrochemical energy storage has the advantages of low environmental pollution, high energy conversion rate, and high specific energy, which has attracted great attention from academia and industry [1–3]. The key to electrochemical energy storage is the reasonable selection and structure design of electrode materials. Transition metal carbides or nitrides named MXenes are a kind of metal-like compounds produced by carbon or nitrides atoms entering the lattice of transition metal, which have the advantages of high hardness, high melting point, and corrosion resistance [4, 5]. MXenes are labeled as $M_{n+1}X_nT_x$ ($n = 1$–3), where M is transition metal, X is carbon or nitrogen, and T represents the surface functional groups (such as -O, -F, and -OH). Due to the large specific surface area and effective diffusion path of ions, two-dimensional MXene materials with unique electronic structure, good chemical stability, and high conductivity, have demonstrated promising potential in the fields of lithium batteries, supercapacitors, and sensors [6, 7]. For instance, Zhao *et al* prepared the MXene/TMO hybrid film electrodes with high reversible capacities over 1200 mAh g^{-1} which performed long cycling stabilities [8]. Wang *et al* synthesized

* Author to whom any correspondence should be addressed.
[5] These authors contributed equally to this work.

MoS_2/Ti_3C_2 MXene heterostructure with an excellent specific capacitance of 386.7 F g^{-1} and outstanding rate performance [9].

It is reported that various MXenes are theoretically predicted and over 20 different MXenes are successfully synthesized [10–12]. Particularly, most of the research has been targeted at titanium carbide (Ti_3C_2) because of its outstanding metallic electrical conductivity and capacitance [13–16]. Hu *et al* investigated the intrinsic electronic conduction properties of $Ti_3C_2(OH)_2$ by dispersion-corrected density functional theory [17]. Miranda *et al* characterized the electronic properties of single-layer $Ti_3C_2T_x$ flakes. It was indicated that the metallic electrical conduction of titanium carbide MXene was still maintained at the monolayer level [18]. Meanwhile, the $Ti_3C_2T_x$ films have excellent tensile strength and Young's modulus, suggesting that it is also capable of producing films with excellent mechanical properties [19]. Zhang *et al* provided a scalable manufacturing method of pure $Ti_3C_2T_x$ MXene films to achieve both high electrical conductivity (1.5×10^6 S m^{-1}) and high tensile strength (570 MPa) [20]. Lukatskaya *et al* fabricated a Ti_3C_2 MXene film with specific capacitance up to 210 F g^{-1} at a high rate capability of 10 V s^{-1}, outperforming the most known carbon supercapacitors [21]. Ling *et al* reported that both pure $Ti_3C_2T_x$ and $Ti_3C_2T_x$/PVA composites exhibited high electrical conductivity as 2.4×10^5 S m^{-1} and 2.2×10^4 S m^{-1} respectively [22].

In contrast to the widely concerned electrical properties, studies on the thermal properties of $Ti_3C_2T_x$ are very limited. The thermal properties are fundamentally important in the application of two-dimensional MXenes materials, and directly affect the performance and lifetime of new devices. In the application of new electronic devices, the existence of high local hot spots can lead to a sharp decrease in the lifetime, weaken the efficiency and safety of the device, and a higher challenge to the thermal stability and thermal conductivity of the material. The $Ti_3C_2T_x$ MXenes are usually applied in a complex environment with temperature variations. It is necessary to study the properties of thermal conductivity varying with temperature. Borysiuk *et al* investigated the thermal stability of 2D titanium carbides by molecular dynamics simulation [23]. But the measurement of free-standing $Ti_3C_2T_x$ films is challenging due to their complex structure, and less work has been reported. Recently, Liu *et al* measured the high thermal conductivity of $Ti_3C_2T_x$ composites to be 55.8 W mK^{-1} by Raman spectroscopy technique, which even surpassed many metals and other two-dimensional materials [24]. Chen *et al* prepared nano-flake $Ti_3C_2T_x$ MXene and the thermal conductivity was determined as 2.8 W mK^{-1} at 290 K using the steady-state T-type method [25]. $Ti_3C_2T_x$ MXenes are usually applied in a complex environment with temperature variations. It is necessary to study the properties of thermal conductivity varying with temperature.

In this work, the temperature dependence of thermal conductivity of $Ti_3C_2T_x$ MXenes is systematically investigated through both experimental and simulation methods. The transient electro-thermal (TET) is employed to characterize the thermal conductivity of $Ti_3C_2T_x$ which is synthesized by the dip-coating method. A simplified single-layer Ti_3C_2 model is established to get a better understanding of the thermal transport in the nanostructure by using molecular dynamic (MD) simulation. Meanwhile, the effect of inner stress on the thermal properties of the titanium carbide is explored. Our experimental and simulation results of the temperature dependence of thermal conductivity would provide informative guidance for the development and application of $Ti_3C_2T_x$ MXenes.

2. Experimental method

2.1. Physical model

Based on one-dimensional transient thermal behavior model, the TET technique is an effective Joule-heating method to characterize the thermal diffusivity and thermal conductivity of conductive wires [26]. As shown in figure 1(a), the sample was placed in suspension between two electrodes and attached with silver paste. The copper electrodes have a good heat dissipation performance and keep the ends of the sample at room temperature (T_0). While the step current heats the sample, the sample undergoes a transient temperature rise and eventually reaches a steady-state thermal equilibrium, as shown in figure 1(b). There is a maximum temperature rise at the midpoint of the sample, while the ends remain at room temperature attached to the heat sink. The direction of heat flow inside the sample is only related to its temperature gradient and is not related to the direction of the heating current. The temperature rise is closely related to the thermal properties of the material, which can be obtained by measuring the voltage signal simultaneously. This entire heating is performed inside the vacuum chamber, so the effect of convective heat transfer is negligible. With the boundary condition, the temperature distribution along the length (x) direction conforms to the one-dimensional thermal conductivity model:

$$\rho C_p \frac{\partial T}{\partial t} = k\frac{\partial^2 T}{\partial x^2} + q_0, \tag{1}$$

where k is the thermal conductivity, ρ is the density, C_p is the specific heat, and q_0 is the heating power per unit volume. The average temperature rise is determined by [26]:

$$T(t) = T_0 + \frac{8q_0L^2}{k\pi^4}\sum_{m=1}^{\infty}\frac{1-\exp[-(2m-1)^2\pi^2\alpha t/L^2]}{(2m-1)^4}, \tag{2}$$

where L is the length of the sample, α is the thermal diffusivity. The normalized temperature rise, defined as $T^*(t) = [T(t) - T_0]/[T(t\to\infty) - T_0]$, can be expressed as:

$$T^* = \frac{96}{\pi^4}\sum\nolimits_{m=1}^{\infty}\frac{1-\exp[-(2m-1)^2\pi^2\alpha t/L^2]}{(2m-1)^4}. \tag{3}$$

The thermal diffusivity can be given by fitting the curve of the T^* with time t in equation (3) when the sample achieves the final steady-state (T_∞), the thermal conductivity k can be calculated as $k = q_0L^2/12(T_\infty - T_0)$.

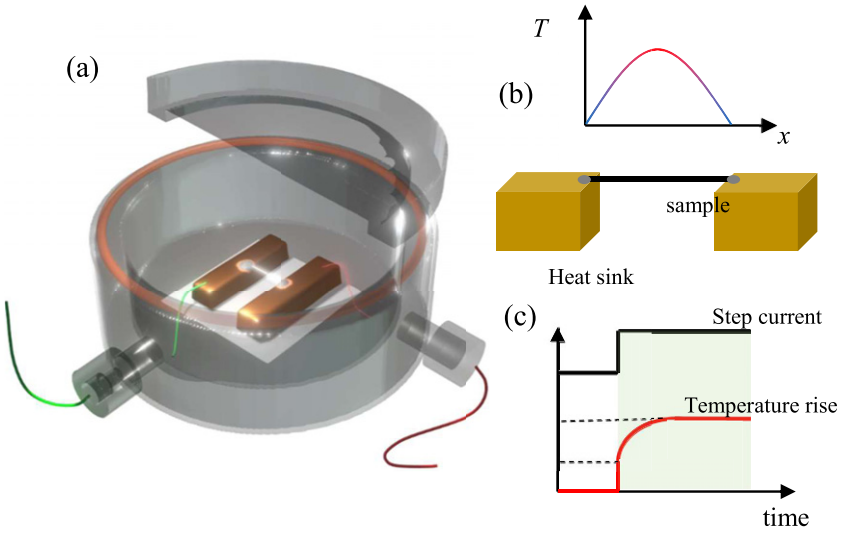

Figure 1. (a) Schematic of experiment setup by TET technique. (b) The physical model of the temperature rises. (c) The process of temperature rise of the sample.

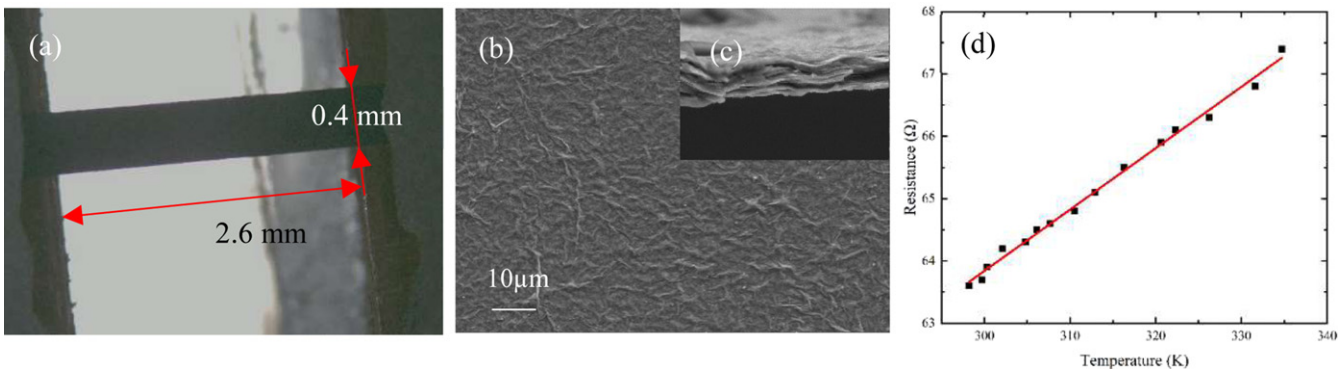

Figure 2. (a) The image of $Ti_3C_2T_x$ sample pasted between heat sinks. The SEM image on (b) top view of $Ti_3C_2T_x$ film, and (c) side view of $Ti_3C_2T_x$ film, (d) the relationship between electrical resistance and temperature of $Ti_3C_2T_x$ sample.

2.2. Experimental details

As shown in figure 2(a), the $Ti_3C_2T_x$ film is prepared into a long strip of 2.6 mm in length, 0.41 mm in width, and 40 μm in thickness. $Ti_3C_2T_x$ sample was prepared using the conventional dip-coating method [14]. The Ti_3AlC_2 was treated with HF at 40°–45° for 48 h under magnetic stirring to dissolve the Al elements. The mixture was processed by ultrasonication and centrifugation to obtain a suspension. After drying and vacuum filtering at room temperature, the $Ti_3C_2T_x$ sample is prepared. The SEM image on the top view and side view of $Ti_3C_2T_x$ film is shown in figures 2(b) and (c). The sample surface is rough due to the stacking of multiple pieces of material, but a clear layered structure can be observed in its thickness direction.

In the experiment, a current source (KEITHLEY 6220) provides step current. The sample is heated in a vacuum chamber under 10^{-3} Torr to eliminate the effect of heat convection. And all measurements are averaged over three times to reduce experimental error. A cooling time is set long enough to ensure that the sample returns to room temperature before the next heating. The temperature rise of the sample is obtained by collecting the voltage signal at both ends of the sample with a data acquisition card (NI USB-6009) during the measurement. The thermal diffusivity of the material is obtained by fitting the voltage change curve with time, while the thermal conductivity is calculated from the average temperature rise. Figure 2(d) illustrates a linear fitting of the resistance versus temperature ranging from 298 K to 335 K with a slope of 0.098 Ω K^{-1}. The resistance temperature coefficient of the material needs to be determined before the experiment.

3. Results and discussion

3.1. Characterization of $Ti_3C_2T_x$ sample

The x-ray diffraction (XRD) patterns of Ti_3AlC_2 (before exfoliation) and $Ti_3C_2T_x$ are shown in figure 3(a). It is shown that the process of exfoliating $Ti_3C_2T_x$ makes part of signal disappear in the out-of-plane direction. Also, ultrahigh pressure and tremendous shear contributed to the broadening of the peak in the XRD patterns of few-layer $Ti_3C_2T_x$ [27]. Previous work reported that the (002) peak at 9.7° corresponds to the basal planes of 2D Ti_3C_2 layers declined compared to

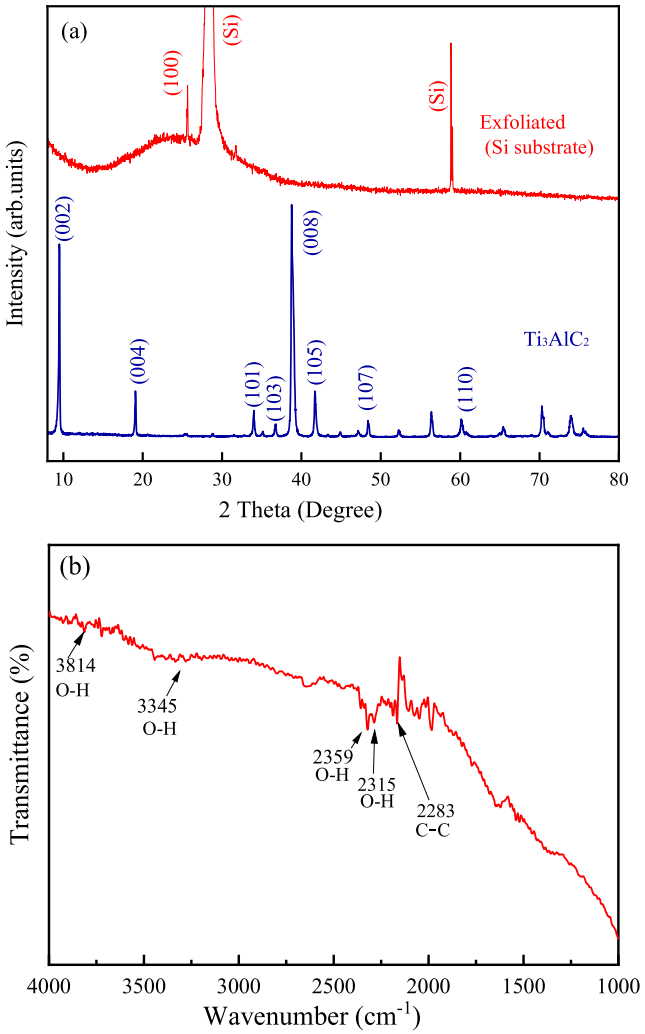

Figure 3. (a) XRD patterns obtained from Ti_3AlC_2 (before exfoliation) and $Ti_3C_2T_x$ sample. (b) FT-IR spectrum of $Ti_3C_2T_x$ sample.

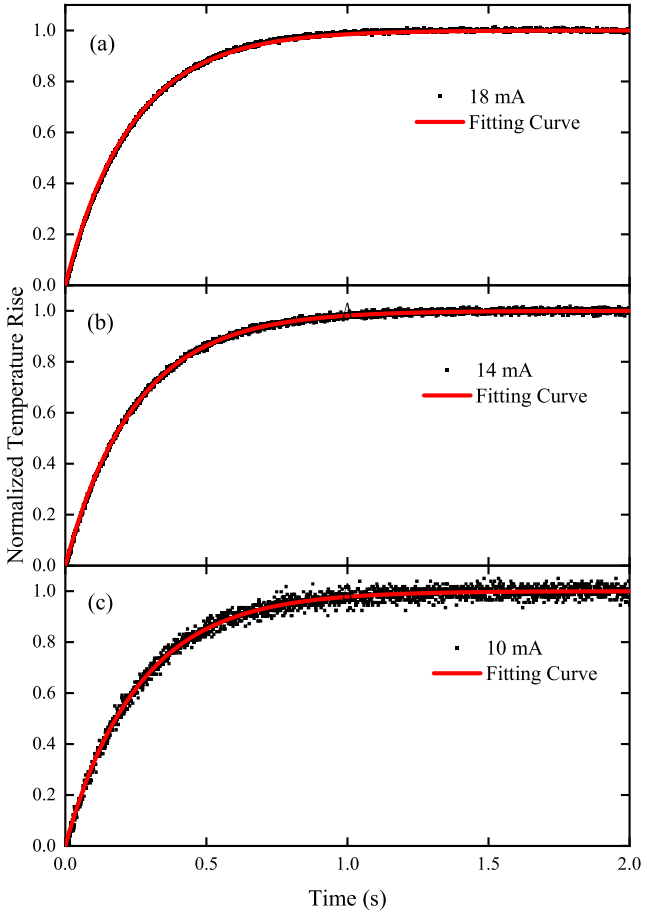

Figure 4. The transient temperature rise of the $Ti_3C_2T_x$ sample at three heating currents (a) 18 mA, (b) 14 mA, and (c) 10 mA.

the (002) peak of non-exfoliated [15, 28]. During the preparation of $Ti_3C_2T_x$ thin film samples, the Al layer needs to be etched using hydrofluoric acid, and pure $Ti_3C_2T_x$ samples are obtained by high-pressure filtration. The (100) peak at 23.4° in the exfoliated sample is corresponding to the -F and -OH function groups. In addition, the peaks appearing at 28.3° and 59.1° belong to Si substrate. The (008) peak at 39.2° disappeared in the exfoliated sample indicates that the HF etching is efficient for the MAX phase. After the exfoliated $Ti_3C_2T_x$ sample was sprayed onto the silicon substrate, the anisotropy of the formed $Ti_3C_2T_x$ film was reduced causing the disappearance of the characteristic peaks.

To characterize the function group on the surface of the $Ti_3C_2T_x$ sample, the FTIR spectrum is shown in figure 3(b). In the FTIR results, the peaks at 2315 cm^{-1}, 2359 cm^{-1}, 3345 cm^{-1}, and 3814 cm^{-1} demonstrate the existence of O–H [29]. The peak at 2283 cm^{-1} reveals the stretching of C–C. The peaks corresponding to the C–F bond are too weak to obtain. That means -OH still exists as the most numerous function group. The disappearance of the peak at 1643 cm^{-1} means that no Al–OH bond was produced after fully etching with HF acid [30]. No significant new absorption peaks were observed in the FT-IR spectrum indicating no impurities were introduced.

3.2. Temperature dependence on thermal properties of $Ti_3C_2T_x$

To explore the variation of thermal properties of $Ti_3C_2T_x$ with temperature, different heating currents are applied to the sample in the experiment (from 10 mA to 19 mA). The relationship between the voltage at both ends of the sample and the heating time can be obtained at different temperatures. The voltage data were averaged by measuring several times at the same current. Figure 4 shows the normalized temperature rise of the $Ti_3C_2T_x$ sample at three heating currents (10 mA, 14 mA, 18 mA). The absolute temperature rise of the sample is smaller at low current, and the fluctuation of the sampled data has a greater impact on the experimental results, while the sampled data is more stable in the case of high current. The sample heats up rapidly during the initial transient temperature rise (within 1 s) and finally reaches a steady state. The thermal diffusivity of the $Ti_3C_2T_x$ sample is obtained by the best fitting curve based on equation (3). And the well-fitting curve shown in figure 4 demonstrate that the influence of contact resistance at both ends of the samples can be neglected. As shown in figure 5, the thermal diffusivity increases from

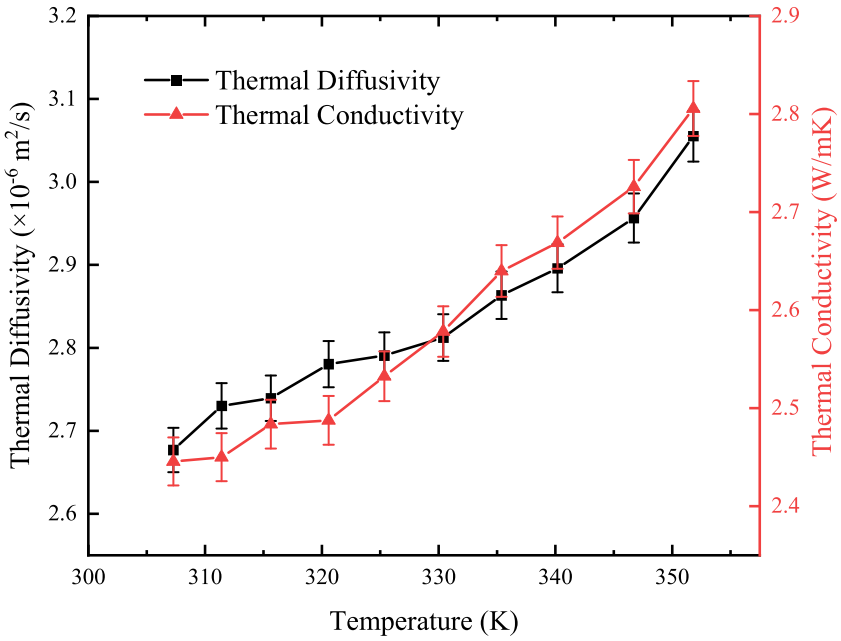

Figure 5. Temperature dependence of thermal diffusivity and thermal conductivity of $Ti_3C_2T_x$ sample.

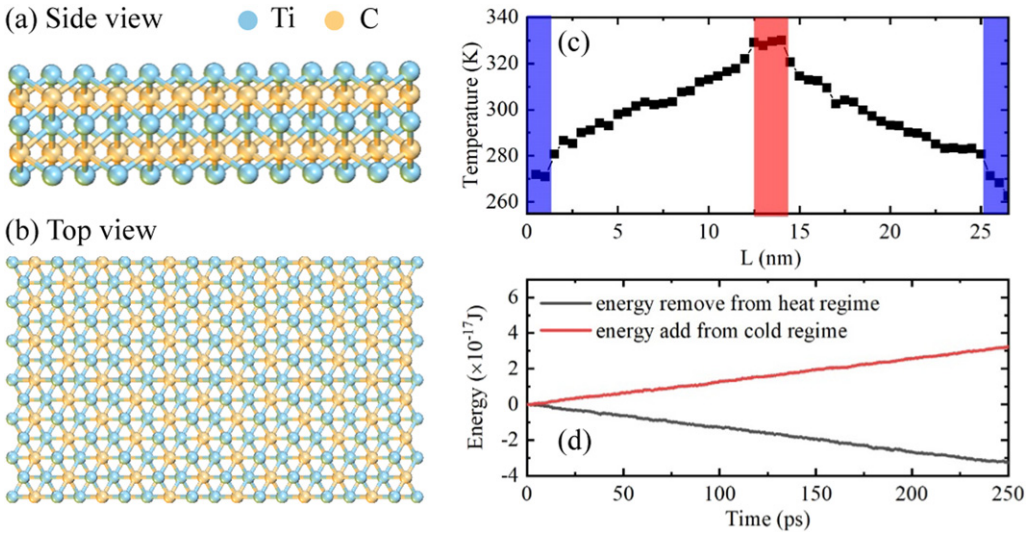

Figure 6. The atomic configurations of Ti_3C_2 (a) side view (b) top view. (c) The steady-state temperature profile in the in-plane direction. (d) The energy balance of heat and cold sources.

2.68×10^{-6} m^2 s^{-1} to 3.06×10^{-6} m^2 s^{-1} as the temperature increases from 307 K to 352 K. According to the steady-state temperature rise, the thermal conductivity is calculated as 2.45 W mK^{-1} at room temperature and 2.81 W mK^{-1} at 352 K, which is in good agreement with the literature value of 2.84 W mK^{-1} at 290 K [25]. The thermal diffusivity α is obtained by fitting the transient temperature rise process in the TET experiment. The thermal conductivity k is obtained by $q_0L^2/12(T_\infty - T_0)$ which is not directly given by the relationship of $k = \alpha\rho C_p$. The thermal diffusivity and thermal conductivity obtained from the two experiments do show a good linear relationship which indicated that the physical properties (heat capacity and density) of the samples are stable during the experiments.

The thermal conductivity of the sample in our experiment is much lower than that of monolayer $Ti_3C_2T_x$ MXenes in simulations [31, 32], which is common in many two-dimensional materials. The sample with a multilayer structure provides more phase-space states for phonon scattering, resulting in a significant decrease in thermal conductivity [33]. A large number of interfacial gaps between $Ti_3C_2T_x$ flakes will further reduce the thermal conductivity of the experimental sample. Meanwhile, the defects are inevitably introduced during the manufacturing process, which is also a negative factor

affecting the heat transfer efficiency of the $Ti_3C_2T_x$ MXenes [34, 35]. A strong phonon scattering induced by the wrinkled nanostructures (as shown in the SEM image) could be an important reason for the reduced thermal conductivity [36, 37].

Since the hot carriers inside the conducting materials are electrons and phonons, the thermal conductivity of the $Ti_3C_2T_x$ sample can be divided into the electrons-contributing part and phonons-contributing part [38]. Determined by the Wiedemann–Franz law, the electron-contributed thermal conductivity can be expressed as $k_e/\sigma = L_0T$, where σ is the electrical conductivity, T is the temperature and L_0 is the constant Lorenz number (2.44×10^{-8} WΩ K^{-2}). Even at the highest experimental temperature, the calculated k_e is 0.02 W mK^{-1} which is less than 1% effect of the measured thermal conductivity. It is indicated that the thermal transport of phonons dominated in our $Ti_3C_2T_x$ sample. The phonons contributed thermal conductivity k_p is known as $k_p = 1/3Cvl$, where l is the mean free path, v is the average group velocity, C is the specific heat capacity [39]. The k_p is mainly influenced by the specific heat capacity at low temperature, which increases with the temperature rising with its peak generally appearing near room temperature. At high temperatures, the influence of phonon scattering gradually dominates leading to the shorter mean free path [40]. Detailed analysis about the monolayer $Ti_3C_2T_x$ material with crystalline structure will be provided in the following section. The combined effects of these two opposite factors ultimately result in an overall enhancement of 16% in the experimentally measured thermal conductivity.

3.3. Physical exploration via MD simulation

A further investigation about the heat transfer mechanism of the $Ti_3C_2T_x$ is conducted by molecular dynamics simulation. The atomic configurations of Ti_3C_2 are illustrated in figures 6(a) and (b). The size of the Ti_3C_2 system is 26.59×3.07 nm^2 ($x \times y$). In these simulations, MEAM potentials are chosen to model the interactions of Ti and C atoms. The periodic boundary condition is performed in both directions. All simulations in this study are used the Large-scale Atomic/Molecular Massively Parallel Simulator (LAMMPS) software. The non-equilibrium molecular dynamics (NEMD) method is utilized to calculate the thermal conductivity of Ti_3C_2. The whole system is firstly relaxed under the isothermal–isobaric ensemble (NPT) 50 ps for eliminating the residual stress. After relaxation, a 500 ps canonical ensemble (NVT) is employed to equilibrium the system at the target temperature. Simulations run under the microcanonical ensemble following. Until the whole system reaches the equilibrium state, three regions are chosen to apply the Langevin thermostat for forming the temperature gradient. The specific regions and the figure of the final temperature gradient are displayed in figures 6(c) and (d).

The temperature difference is set as 60 K and the heat flux transport from the hot region which is located at the middle of the Ti_3C_2 materials to the cold regions which are located at the two sides. The energy variation of both regions is calculated to certify the final quasi-equilibrium state. If the quasi-equilibrium state is established, the added energy into heat sinks is equal to the removed energy from the heat source which can be seen in figure 6. After that, the thermal conductivity can be calculated by the Fourier's law of thermal conductivity: $Q = k \cdot A \cdot \mathrm{d}T/\mathrm{d}x$, where Q is the heat flux which can be obtained from the fitting of the energy varied with time. A is the area that is the product of thickness and width. The thickness is 0.8 nm and the width is 3.07 nm in this study. The thickness of the monolayer Ti_3C_2 is an intrinsic parameter and can be calculated by *ab initio* calculation [31]. $\mathrm{d}T/\mathrm{d}x$ represents the temperature gradient which can be directly obtained from the division of the temperature difference between the heat source and heat sink and the length of the materials.

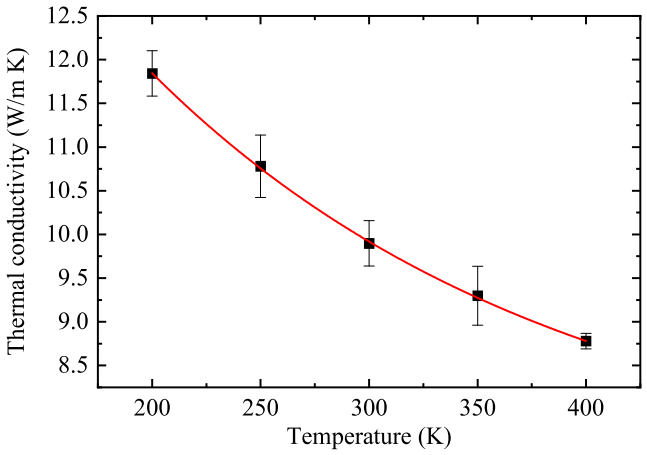

Figure 7. The thermal conductivity of Ti_3C_2 model concerning temperature in MD simulation.

2D materials confront the enormous temperature change in the electronic device [41, 42]. Similar to experiments, the effects of temperature are considered. The thermal conductivity varied with the temperature from 200 K to 600 K is calculated. And the result is depicted in figure 7. A clear tendency can be found while the value of thermal conductivity is 8.77 W mK^{-1} at 400 K and the maximum value is 11.84 W mK^{-1} at 200 K. This tendency is consistent with the study of other 2D materials about the temperature influence in thermal conductivity [33, 43]. The increasing temperature results in the broader phonon density of the state spectrum which means the activated higher frequency phonons. In addition, it also enhances the Umklapp scattering of in-plane phonons which led to the decrease of the mean free path. Although the ascensional range of temperature in experiments is far smaller than that of simulations, it can be deduced that the increased temperature causes the decrease of thermal conductivity, which is an opposite trend compared to the experimental results. The experimental sample is more complicated than the systems of simulations. There is only a single layer in simulation systems, but a multi-layer stacking structure could be found (as shown in the SEM image) in our $Ti_3C_2T_x$ sample. The structure between Ti_3C_2 layers is not alignment which can be diagonal or orthogonal.

The increase of thermal conductivity based on the experiments in this study not only is influenced by temperature but numerous factors are also combined to affect the final experimental results, like stress, out-of-plane heat transportation, and

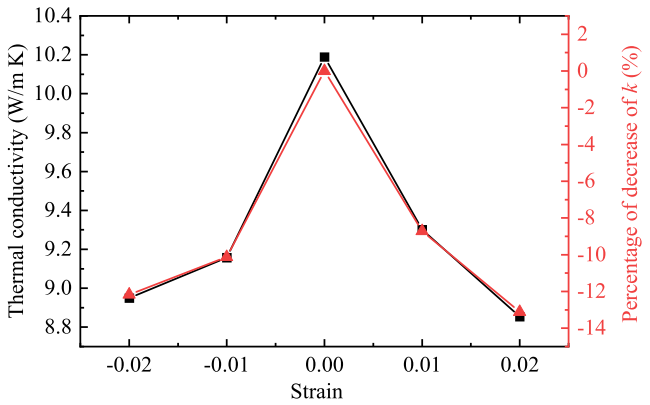

Figure 8. The thermal conductivity as a function of strain.

roughness. Thus, we furtherly calculated the thermal conductivity under the effects of stress. In the setup of MD simulation. We change the deformation variables by up to ±2% in the planar direction (*x* and *y* directions) along the monolayer Ti_3C_2. The relationship between stress and thermal conductivity is illustrated in figure 8. The diminished influence of stress can be observed no matter tensile stress or compressive stress. The decrease percentage compared to the thermal conductivity of a perfect structure without stress is also displayed in figure 8. While the stress is equal to 0.02, the value of thermal conductivity decreases by 13.11%. As for −0.02, the decrease percentage is 12.16%. These results are consistent with the past research [44]. The stress weak the vibration of the atoms causes the decrease of thermal conductivity [45]. In addition, the stress lowers the frequency of high-frequency phonon which softens the phonon models [46]. It intensified the scattering of phonons and results in the decrease of thermal conductivity. In experiments, the structure of the $Ti_3C_2T_x$ thin-film material used in the experiments is more complex than the monolayer of Ti_3C_2 used in the MD simulations. For example, the spatially wrinkled and stacked structure is caused by residual stresses from the processes in the preparation [5]. The increasing temperature improves the distribution of stresses in the lower temperature rise range, which eventually leads to an increase in the thermal conductivity.

4. Conclusions

The temperature dependence on the thermal conductivity of $Ti_3C_2T_x$ MXenes film is comprehensively investigated in this work. With the temperature varying from 307 K to 352 K, the thermal conductivity measured by the TET method increases from 2.45 W mK^{-1} to 2.81 W mK^{-1}, while the thermal diffusivity increases from 2.68 × 10^{-6} m^2 s^{-1} to 3.06 × 10^{-6} m^2 s^{-1}. The electrical resistance also has a temperature-dependence behavior, but the electron-contributed thermal conductivity is calculated to be negligible. The combined effect of increasing specific heat capacity and decreasing mean free path ultimately results in an overall enhancement of 16% in the measured thermal conductivity. The Umklapp scattering of in-plane phonons which led to the decrease of the mean free path is investigated by MD simulation. The tendency can be found while the value of thermal conductivity is 8.77 W mK^{-1} at 400 K and the maximum value is 11.84 W mK^{-1} at 200 K. Furthermore, the effect of possible changes in internal stresses on the thermal conductivity is analyzed. Stress release from the wrinkle nanostructure during the temperature rise process is proven to enhance the thermal conductivity. Combined with a comprehensive analysis of the temperature characteristics and intrinsic mechanism, the experimental and simulation results provide informative guidance for the development and application of $Ti_3C_2T_x$ MXenes.

Acknowledgments

The authors acknowledge the financial support from the National Key Research and Development Program of China (No. 2019YFE0119900), the National Natural Science Foundation of China (No. 52076156), and Fundamental Research Funds for the Central Universities (No. 2042020kf0194). The authors appreciate the support from the Supercomputing Center of Wuhan University.

Data availability statement

All data that support the findings of this study are included within the article (and any supplementary files).

ORCID iDs

Huan Lin https://orcid.org/0000-0002-6475-0842
Yanan Yue https://orcid.org/0000-0002-3489-3949

References

[1] Sarycheva A, Polemi A, Liu Y, Dandekar K, Anasori B and Gogotsi Y 2018 2D titanium carbide (MXene) for wireless communication *Sci. Adv.* **4** eaau0920
[2] Ahmed B, Anjum D H, Gogotsi Y and Alshareef H N 2017 Atomic layer deposition of SnO_2 on MXene for Li-ion battery anodes *Nano Energy* **34** 249–56
[3] Anasori B, Lukatskaya M R and Gogotsi Y 2017 2D metal carbides and nitrides (MXenes) for energy storage *Nat. Rev. Mater.* **2** 16098
[4] Aslam M K and Xu M 2020 A mini-review: MXene composites for sodium/potassium-ion batteries *Nanoscale* **12** 15993–6007
[5] Naguib M, Mochalin V N, Barsoum M W and Gogotsi Y 2014 25th anniversary article: MXenes: a new family of two-dimensional materials *Adv. Mater.* **26** 992–1005
[6] Xu G, Wang X, Gong S, Wei S, Liu J and Xu Y 2018 Solvent-regulated preparation of well-intercalated $Ti_3C_2T_x$ MXene nanosheets and application for highly effective electromagnetic wave absorption *Nanotechnology* **29** 355201
[7] Wu C-W, Unnikrishnan B, Chen I W P, Harroun S G, Chang H-T and Huang C-C 2020 Excellent oxidation resistive MXene aqueous ink for micro-supercapacitor application *Energy Storage Mater.* **25** 563–71
[8] Zhao M-Q, Torelli M, Ren C E, Ghidiu M, Ling Z, Anasori B, Barsoum M W and Gogotsi Y 2016 2D titanium carbide and

transition metal oxides hybrid electrodes for Li-ion storage *Nano Energy* **30** 603–13
[9] Wang X *et al* 2020 2D/2D 1T-MoS_2/Ti_3C_2 MXene heterostructure with excellent supercapacitor performance *Adv. Funct. Mater.* **30** 0190302
[10] Kim H, Wang Z and Alshareef H N 2019 MXetronics: electronic and photonic applications of MXenes *Nano Energy* **60** 179–97
[11] Michael J, Qifeng Z and Danling W 2019 Titanium carbide MXene: synthesis, electrical and optical properties and their applications in sensors and energy storage devices *Nanomater. Nanotechnol.* **9** 184798041882447
[12] Zhong Y, Xia X, Shi F, Zhan J, Tu J and Fan H J 2016 Transition metal carbides and nitrides in energy storage and conversion *Adv. Sci.* **3** 1500286
[13] Yang C, Tang Y, Tian Y, Luo Y, He Y, Yin X and Que W 2018 Achieving of flexible, free-standing, ultracompact delaminated titanium carbide films for high volumetric performance and heat-resistant symmetric supercapacitors *Adv. Funct. Mater.* **28** 1705487
[14] Salles P, Pinto D, Hantanasirisakul K, Maleski K, Shuck C E and Gogotsi Y 2019 Electrochromic effect in titanium carbide MXene thin films produced by dip-coating *Adv. Funct. Mater.* **29** 1809223
[15] Kong A *et al* 2021 Synergetic control of Ru/MXene 3D electrode with superhydrophilicity and superaerophobicity for overall water splitting *Chem. Eng. J.* **426** 131234
[16] Kong A, Sun Y, Peng M, Gu H, Fu Y, Zhang J and Li W 2021 Amino-functionalized MXenes for efficient removal of Cr (VI) *Colloids Surf.* A **617** 126388
[17] Hu T, Zhang H, Wang J, Li Z, Hu M, Tan J, Hou P, Li F and Wang X 2015 Anisotropic electronic conduction in stacked two-dimensional titanium carbide *Sci. Rep.* **5** 16329
[18] Miranda A, Halim J, Barsoum M W and Lorke A 2016 Electronic properties of freestanding $Ti_3C_2T_x$ MXene monolayers *Appl. Phys. Lett.* **108** 033102
[19] Lipatov A, Lu H, Alhabeb M, Anasori B, Gruverman A, Gogotsi Y and Sinitskii A 2018 Elastic properties of 2D $Ti_3C_2T_x$ MXene monolayers and bilayers *Sci. Adv.* **4** eaat0491
[20] Zhang J *et al* 2020 Scalable manufacturing of free-standing, strong $Ti_3C_2T_x$ MXene films with outstanding conductivity *Adv. Mater.* **32** 2001093
[21] Lukatskaya M R *et al* 2017 Ultra-high-rate pseudocapacitive energy storage in two-dimensional transition metal carbides *Nat. Energy* **2** 17105
[22] Ling Z, Ren C E, Zhao M-Q, Yang J, Giammarco J M, Qiu J, Barsoum M W and Gogotsi Y 2014 Flexible and conductive MXene films and nanocomposites with high capacitance *Proc. Natl Acad. Sci.* **111** 16676–81
[23] Borysiuk V and Mochalin V N 2019 Thermal stability of two-dimensional titanium carbides $Ti_{n+1}C_n$ (MXenes) from classical molecular dynamics simulations *MRS Commun.* **9** 203–8
[24] Liu R and Li W 2018 High-thermal-stability and high-thermal-conductivity $Ti_3C_2T_x$ MXene/poly(vinyl alcohol) (PVA) composites *ACS Omega* **3** 2609–17
[25] Chen L, Shi X, Yu N, Zhang X, Du X and Lin J 2018 Measurement and analysis of thermal conductivity of $Ti_3C_2T_x$ MXene films *Materials* **11** 1701
[26] Guo J, Wang X and Wang T 2007 Thermal characterization of microscale conductive and nonconductive wires using transient electrothermal technique *J. Appl. Phys.* **101** 063537
[27] Naguib M, Kurtoglu M, Presser V, Lu J, Niu J, Heon M, Hultman L, Gogotsi Y and Barsoum M W 2011 Two-dimensional nanocrystals produced by exfoliation of Ti_3AlC_2 *Adv. Mater.* **23** 4248–53
[28] Kang R *et al* 2019 Enhanced thermal conductivity of epoxy composites filled with 2D transition metal carbides (MXenes) with ultralow loading *Sci. Rep.* **9** 1–14
[29] Lu X, Huang H, Zhang X, Lin P, Huang J, Sheng X, Zhang L and Qu J-P 2019 Novel light-driven and electro-driven polyethylene glycol/two-dimensional MXene form-stable phase change material with enhanced thermal conductivity and electrical conductivity for thermal energy storage *Composites* B **177** 107372
[30] Khan A A, Tahir M and Bafaqeer A 2020 Constructing a stable 2D layered Ti_3C_2 MXene cocatalyst-assisted TiO_2/g-C_3N_4/Ti_3C_2 heterojunction for tailoring photocatalytic bireforming of methane under visible light *Energy Fuels* **34** 9810–28
[31] Gholivand H, Fuladi S, Hemmat Z, Salehi-Khojin A and Khalili-Araghi F 2019 Effect of surface termination on the lattice thermal conductivity of monolayer $Ti_3C_2T_z$ MXenes *J. Appl. Phys.* **126** 065101
[32] Guo Z, Miao N, Zhou J, Pan Y and Sun Z 2018 Coincident modulation of lattice and electron thermal transport performance in MXenes via surface functionalization *Phys. Chem. Chem. Phys.* **20** 19689–97
[33] Balandin A A 2011 Thermal properties of graphene and nanostructured carbon materials *Nat. Mater.* **10** 569
[34] Sang X, Xie Y, Lin M-W, Alhabeb M, Van Aken K L, Gogotsi Y, Kent P R C, Xiao K and Unocic R R 2016 Atomic defects in monolayer titanium carbide ($Ti_3C_2T_x$) MXene *ACS Nano* **10** 9193–200
[35] Yasaei P, Tu Q, Xu Y, Verger L, Wu J, Barsoum M W, Shekhawat G S and Dravid V P 2019 Mapping hot spots at heterogeneities of few-layer Ti_3C_2 MXene sheets *ACS Nano* **13** 3301–9
[36] Cui L, Du X, Wei G and Feng Y 2016 Thermal conductivity of graphene wrinkles: a molecular dynamics simulation *J. Phys. Chem.* C **120** 23807–12
[37] Ma W G, Wang H D, Zhang X and Wang W 2010 Experiment study of the size effects on electron–phonon relaxation and electrical resistivity of polycrystalline thin gold films *J. Appl. Phys.* **108** 409
[38] Kurnia F, Seidel J, Hart J N and Valanoor N 2021 Optical tuning of resistance switching in polycrystalline gallium phosphide thin films *J. Phys. Chem. Lett.* **12** 2327–33
[39] Pang J W, Buyers W J, Chernatynskiy A, Lumsden M D, Larson B C and Phillpot S R 2013 Phonon lifetime investigation of anharmonicity and thermal conductivity of UO_2 by neutron scattering and theory *Phys. Rev. Lett.* **110** 157401
[40] Maradudin A and Fein A 1962 Scattering of neutrons by an anharmonic crystal *Phys. Rev.* **128** 2589
[41] Liu J, Wang H, Hu Y, Ma W and Zhang X 2015 Laser flash-Raman spectroscopy method for the measurement of the thermal properties of micro/nano wires *Rev. Sci. Instrum.* **86** 014901
[42] Li Q-Y, Xia K, Zhang J, Zhang Y, Li Q, Takahashi K and Zhang X 2017 Measurement of specific heat and thermal conductivity of supported and suspended graphene by a comprehensive Raman optothermal method *Nanoscale* **9** 10784
[43] Cai W, Moore A L, Zhu Y, Li X, Chen S, Shi L and Ruoff R S 2010 Thermal transport in suspended and supported monolayer graphene grown by chemical vapor deposition *Nano Lett.* **10** 1645–51
[44] Zhang C, Hao X-L, Wang C-X, Wei N and Rabczuk T 2017 Thermal conductivity of graphene nanoribbons under shear deformation: a molecular dynamics simulation *Sci. Rep.* **7** 1–8
[45] Li X, Maute K, Dunn M L and Yang R 2010 Strain effects on the thermal conductivity of nanostructures *Phys. Rev.* B **81** 245318
[46] Ma F, Zheng H, Sun Y, Yang D, Xu K and Chu P K 2012 Strain effect on lattice vibration, heat capacity, and thermal conductivity of graphene *Appl. Phys. Lett.* **101** 111904